CHINESE OPTICS LETTERS

Vol. 19, No. 8 | August 2021

Design of a single-mode directly modulated orbital angular momentum laser

Xiang Ma (马 向), Shuang Zheng (郑 爽), Jia Liu (刘 佳), Quanan Chen (陈泉安), Qiaoyin Lu (陆巧银), and Weihua Guo (国伟华)*

Wuhan National Laboratory for Optoelectronics & School of Optical and Electronic Information, Huazhong University of Science and Technology, Wuhan 430074, China

*Corresponding author: guow@hust.edu.cn

Received October 16, 2020 | Accepted January 5, 2021 | Posted Online April 22, 2021

We propose a design of single-mode orbital angular momentum (OAM) beam laser with high direct-modulation bandwidth. It is a microcylinder/microring cavity interacted with two types of second-order gratings: the complex top grating containing the real part and the imaginary part modulations and the side grating. The side grating etched on the periphery of the microcylinder/microring cavity can select a whispering gallery mode with a specific azimuthal mode number, while the complex top grating can scatter the lasing mode with travelling-wave pattern vertically. With the cooperation of the gratings, the laser works with a single mode and emits radially polarized OAM beams. With an asymmetrical pad metal on the top of the cavity, the OAM on-chip laser can firstly be directly modulated with electrical pumping. Due to the small active volume, the laser with low threshold current is predicted to have a high direct modulation bandwidth about 29 GHz with the bias current of ten times the threshold from the simulation. The semiconductor OAM laser can be rather easily realized at different wavelengths such as the O band, C band, and L band.

Keywords: orbital angular momentum; diffraction and gratings; vertical emitting lasers; microcavity devices; semiconductor lasers; single mode; directly modulated laser.

DOI: 10.3788/COL202119.081401

1. Introduction

With the exponentially growing demand of data traffic capacity, orbital angular momentum (OAM)-carrying beams have attracted great interests for its topological helical phase fronts. OAM has been considered as an additional degree of freedom of a photon or light beam having the potential to obtain greater information capacity and can be widely applied into photonic integrated technologies[1]. OAM-carrying light owns $l\hbar$ per photon (l is the topological charge and $\hbar$ is the reduced Planck constant). Here, l can be any integer so that the new dimensionality is infinite. Beams carrying OAM are extremely appealing research for their varieties of applications such as free-space telecommunications, optical manipulation, and quantum information[2-4]. Generating OAM beams is highly desired[5,6] and challenging especially for active integrated devices with electrical pump.

Microcavities such as microdisks, microrings and microcylinders, supporting whispering gallery modes (WGMs), are normally used to generate OAM beams[7-10]. Recently, several passive OAM emitters for applications in optical communication have been demonstrated on silicon substrate[9,10]. However, the passive OAM generators will need additional optical sources, which limit their prospect because of additional cost and devices. An OAM vertical surface emitting laser[11] was put forward by fabricating micro-scale spiral phase plates upside a vertical-cavity surface-emitting laser, but its fabrication cannot be realized using normal plane-etching steps in semiconductor fabrications. Contemporarily, an OAM beam laser was presented[12] using complex refractive index modulation to realize unidirectional circulation for WGMs and additional grating etched on the periphery of the cavity to emit OAM beams. Despite the laser has shown impressive idea, optical pumping needs other optical devices to pump. In addition, the active region is on the top of the cavity, which will introduce extra surface recombination. Afterwards, an OAM beam emitter has been reported, which is a distributed feedback laser integrated with a passive vortex beam component. Although the integrated lasers have shown impressive performance, there is no high-speed directly modulated OAM beam laser until now.

We have put forward a high-speed directly modulated cylindrical vector (CV) beam laser and demonstrated it experimentally[13,14]. The laser emits radially polarized vector beams vertically, and shows high speed direct modulation. However,

the laser emits standing-wave mode, which will limit the applications. To make up the inadequacy of the schemes mentioned above, we propose and design a new single-mode radially polarized OAM beam laser with high direct-modulation bandwidth. This paper is organized as the following: section 2 introduces the device structure and modelling; section 3 explains how the gratings interact with WGMs in the cavity; section 4 provides the numerical simulations and results including the mode selection and the emission patterns; in section 5 the laser characteristics are shown; in the last section we give the conclusion.

2. Device Design and Theory

Figures 1(a) and 1(b) show the schematic structures of the single-mode high-speed directly modulated OAM beam laser. The detailed distributions of the gratings are shown in Fig. 1(c). From top to bottom, the device structure includes the N ohmic contact layer, the grating layer, the upper cladding layer, the active region, the lower cladding layer, the P ohmic contact layer, and the substrate.

To strengthen the interaction of the top gratings and WGMs of the cavity, a thin upper cladding layer is set. N-I-P structure is adopted to decrease the resistance of the laser. The active region includes five compressively strained quantum wells sandwiched between the upper and lower 100 nm optical confinement layers with the same quaternary material. The thickness of every quantum well and barrier is 6 nm and 10 nm, respectively. An InGaAlAs/InP wafer with high differential gain grown on a semi-insulating InP substrate is used for the laser which is easier to realize high-speed modulation. To improve the current injection efficiency, proton is implanted into the P-doped lower cladding layer so as to form a cylinder area with high resistance right below the active region as shown in Fig. 2. With the ion implanted region, the high-order radial WGMs would be inhibited as well. To radiate travelling-wave mode with helical phase fronts, an imaginary part index modulation is introduced to the top grating.

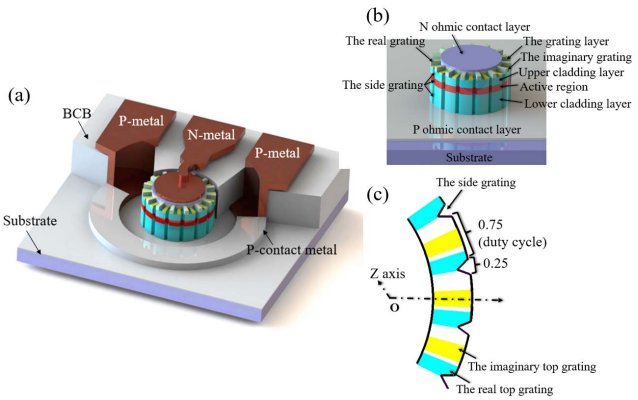

Fig. 1. (a) Schematic structure of the fabricated single-mode high-speed directly modulated OAM beam laser; (b) structure of the laser; (c) distribution of the gratings.

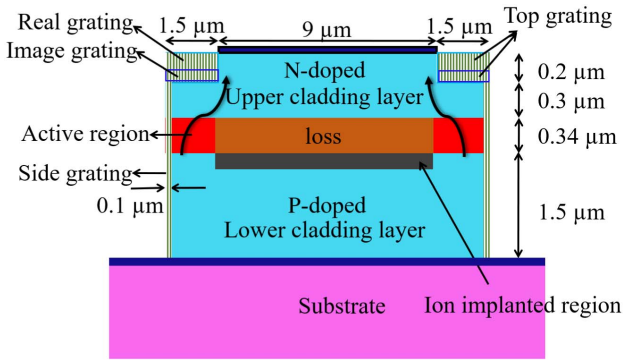

Fig. 2. Cross section of the modelling of the single-mode OAM laser.

Different from the CV beam laser, the cavity of the OAM beam laser here is a microcylinder added with two types of second-order gratings on the top called the top gratings. In this case, the top gratings and the side gratings will not have a symmetry plane any more. The top gratings contain the real part and the imaginary part modulation of the mode refractive index[15]. When the amplitude of the real and imaginary part modulation is equal and the position shifts in the azimuthal direction, the laser could emit unidirectional helical beams. Another second-order grating etched on the external sidewall of the cylinder cavity called as the side grating can select a specific radially polarized standing-wave mode[13]. Distributions of the gratings are depicted in a plane as shown in Fig. 1(c). The whole structure is surrounded by benzocyclobutene (BCB) to decrease the extra parasitic capacitance, which is profitable for high-speed direct modulation.

The cross section of the theoretical model of the OAM beam laser with simulated parameters is shown in Fig. 2 in detail. Outer radii of the N-ohmic contact layer and the cavity are 4.5 and 6 μm, respectively. With the high-resistance ion implantation region, the injected carriers will overlap with mode area of the WGMs adequately and the path of the current flow is pointed out in Fig. 2. An imaginary part of the refractive index is added to the center of the active region on behalf of some absorption loss coming from the N ohmic contact.

E_r and E_φ, along the radial and tangential direction, serve as the two major electrical field components of the transverse-electrical (TE) WGM of the microcylinder cavity. The typical distributions of E_r and E_φ are shown in Fig. 3. Therefore, the top grating and the side grating would interact mainly with E_r and E_φ, respectively.

When the side grating is etched on the periphery of the microcylinder cavity, it would interact mainly with E_φ because it is larger than E_r at the periphery of the cylinder. With the side grating added, the WGMs will be reorganized into symmetrical mode or anti-symmetrical mode (defined for the electric vector), relative to a symmetry plane[16]. The symmetrical mode with the azimuthal mode number (m) equal to the period number of the side grating (N) could perfectly cancel out the scattering loss from E_φ and then have minimum loss. The side grating can select the symmetrical mode with $m = N$ to be the lasing mode,

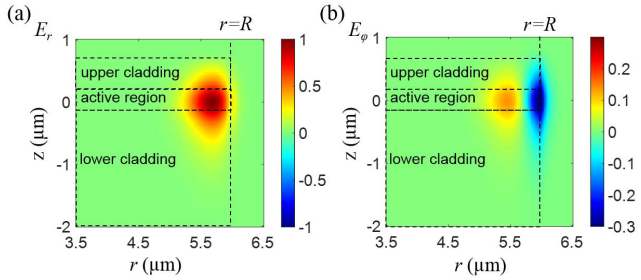

Fig. 3. Typical distributions of the major electrical field components (a) E_r and (b) E_φ of the WGMs in the cross section of the microcylinder cavity.

which only scatters few radially polarized beams from E_r[13]. From our previous research, with higher duty cycle of the side grating, the scattering loss of the lasing mode becomes lower[13]. Here, the side grating is set to be a triangle-shape etched pattern. Duty cycle (unetched part) of 0.75 defined in Fig. 1(c) is preferred here in order to decrease the scattering loss and also reduce difficulty of fabrication.

In this case, the lasing mode selected by the side grating is a standing-wave mode with little corresponding standing-wave emission. Therefore, another mechanism is introduced for emitting travelling-wave field.

Similar to the CV beam laser, a top grating is used for efficient surface-emission. To form travelling-wave emission, the top grating should break the symmetry of the previous cavity with the side grating. The top gratings here include the real part and the imaginary part, which can modulate the real and imaginary parts of the mode refractive index, respectively. The number of the period of the top gratings is M. Hypothetically, the real and the imaginary parts of the modulated refractive index are described as follows:

$$\Delta n = C\cos\varphi + Ci\sin\varphi,$$
$$2\pi p/M \le \varphi \le (p+1/4)2\pi/M,\ p = 0,1,2,3\ldots, \quad (1)$$

where C represents the scale of the modulation of index, φ is the angle along the periphery direction, and p is an integer. This can be spread into all the periods:

$$\Delta n = C_0 + C_\varphi \exp(i\varphi) + C_{-\varphi}\exp(-i\varphi). \quad (2)$$

From Eqs. (1) and (2), we can conclude that $C_{-\varphi}$ equals zero[10]. As a result, if the modulated real part equals the imaginary part of the mode refractive index, only clockwise or anticlockwise WGMs could be scattered out of the microcavity vertically. The scattered electrical field from the WGMs that are radially polarized OAM beams in the vertical direction can be described as

$$\boldsymbol{E}_{\text{emission}} = B\begin{pmatrix}\cos\varphi\\ \sin\varphi\end{pmatrix}\exp[i(M-m)\varphi], \quad (3)$$

where B is the strength of the emission, and $\exp[i(M-m)\varphi]$ expresses the emission carrying OAM beams.

The side grating will introduce serious scattering loss for all WGMs except one mode with $m = N$, and the scattering loss is much larger than from the top grating[13]. Then it is predicted that the side grating can select a standing-wave mode to lase and the top gratings can scatter the mode unidirectionally in the vertical direction to form travelling-wave output. Then with the cooperation of the second-order gratings, the emission of the laser will be radially polarized OAM beams taking the order $l = M - N$. From this analysis, the real part modulation can be easily fabricated by directly etching the upper cladding layer (the grating layer) and the imaginary part modulation can be obtained by means of introducing scattering loss like using some metal materials.

It is proved that the introduced refractive index modulation for the real part can be 0.2 μm-depth etched InP and for the imaginary part can be 45 nm-thickness deposited absorbing metal material germanium (Ge) with the finite element method[17]. Although the imaginary part will also introduce some real part modulation, it will not have a negative effect on generating OAM beams.

3. Simulation and Discussion

The three-dimensional (3D) finite-difference time-domain (FDTD) method[18] is used for simulation of the microcavity interacted with gratings[13]. Several broadband Gaussian pulse sources in the time domain are added to the field component H_z close to the periphery of the microcylinder cavity to excite TE WGMs as many as possible. The variation of a specific field component with time is recorded as the FDTD output, which is transformed into the frequency domain through the Padé approximation transform method[19]. Then the mode resonant frequency and Q factor can be obtained through Lorentzian fitting of the frequency spectrum. To find the mode distribution and the emission pattern, the elongated excitation pulse with the found frequency in the time domain is used for simulation again. To separate the degenerate modes with same mode frequencies of microcavity for only the side grating case, different symmetry conditions are adopted.

The microcylinder cavity interacted with only the side grating is analyzed first using 3D-FDTD method. The number of the grating periods N is 86 in the simulation. The duty cycle of the triangle-shaped side grating is 0.75. The calculated Q factors of the WGMs versus different m close to $N = 86$ are shown in Fig. 4(a). Mode splitting is obvious for the WGMs with $m = N$. The symmetrical mode with $m = N$ has the highest Q factor, much higher than the others, while the anti-symmetrical mode with $m = N$ has the lowest Q factor. Other WGMs are still degenerate and their scattering loss is just between the splitting modes. Therefore, the symmetrical mode with $m = N$ will become the lasing mode. The electrical field distributions of the symmetrical mode and the anti-symmetrical mode are shown in Figs. 4(b) and 4(c).

Then, we simulate the cavity added with both the side grating and the complex top gratings. From the above analysis, when the top gratings are added onto the microcylinder, the cavity will not have the symmetry plane any more. Therefore, in the simulation,

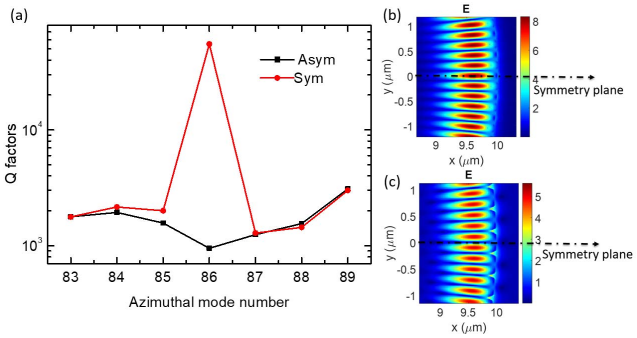

Fig. 4. (a) Q factors of WGMs of the cavity added with only the side grating versus the azimuthal mode number; electrical field distributions of (b) the symmetrial mode and (c) the anti-symmetrical mode.

the symmetry boundary conditions should not be used in this case. When $M = 85$ and $N = 86$, the WGMs with the azimuthal mode number m around N are excited as many as possible and the normalized spectral distribution of the TE WGMs in the vicinity of 1.3 μm is shown in Fig. 5. From the spectrum, only one mode has the narrowest line width (highest Q factor) and becomes the lasing mode, while all the other modes have much wider line width (much lower Q factors). Therefore, the laser reveals an ideal single mode lasing characteristic within the range of 100 nm. With further simulation, the lasing mode is proved to be the mode with $m = N$, because mode selection is mainly determined by the side grating.

The near-electric-field intensity distributions of the lasing modes with $l = M - N = -1$ and $m = N$ above the top grating are shown in Fig. 6. Three different types of the top gratings are considered for comparison, i.e., both the real and the imaginary part modulated grating, only the real part modulated grating, and only the imaginary part modulated grating. In the first case, the distribution of the electric field intensity has nearly no dependence on φ as shown in Fig. 6(a). The electric field intensity components in x and y directions (amount to the electric field passing through a polarizer with 0° and 90°) show vortex

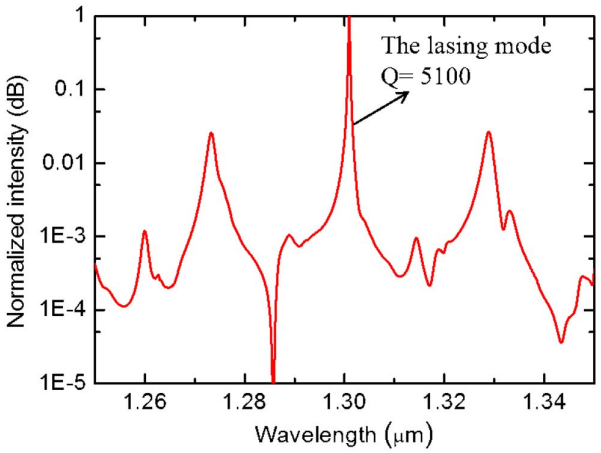

Fig. 5. Spectral distribution of the TE WGMs of the OAM laser with $l = -1$.

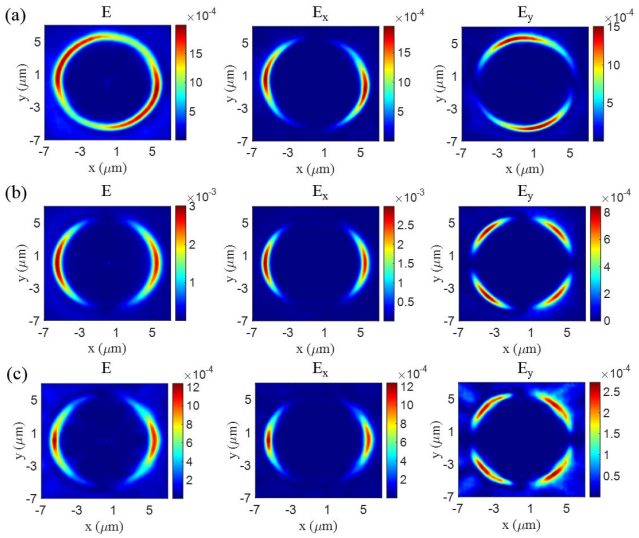

Fig. 6. Near-field intensity distributions of the laser above the top grating, where the period number of the side grating $N = 86$ and that of the top grating $M = 85$. From the top to bottom row are three cases: (a) both the real and the imaginary grating, (b) only the real grating, and (c) only the imaginary grating are added to the microcylinder cavity and serve as the top grating.

beams. The emission of the first case can be described as $\exp i\varphi$. However, in the second case, the electric intensity has a dependence on φ and the emission can be expressed as $\cos\varphi$ as shown in Fig. 6(b). The distribution of the electric field intensity of the third case is similar to the second case as shown in Fig. 6(c). The first case can be regarded as a combination of the second and the third cases, i.e., $\exp i\varphi = \cos\varphi + i\cos(\pi/2 - \varphi)$ for the complex top grating. The real part and the imaginary part of the modulated refractive index have a shift in the φ direction. Therefore, only the complex top grating can radiate travelling OAM-carrying beams. For only the real or the imaginary part of the modulated-index grating situations, standing-wave modes will be scattered. It is testified that the radiated electric field intensity from the OAM beam laser is radially polarized and has nearly no dependence on φ ($E_x \propto \cos\varphi$, $E_y \propto \sin\varphi$) while two other cases have the dependence.

The far-field intensity distributions and phase patterns of the OAM beam lasers above the top gratings in the vertical direction simulated by 3D FDTD method are shown in Figs. 7(a) and 7(b). Different orders l from −2 to 2 with $N = 86$ are displayed. The radiated vortex beam with order of l can be decomposed into a right-handed circularly polarized beam with $l + 1$ and a left-handed circularly polarized beam with $l - 1$[10]. Therefore, far-field intensity of the laser with $l = 0$ shows a donut pattern and that with $l = 1$ or $l = -1$ shows the hot-spot in the center.

The field pattern and spiral pattern of the radiated emission can be modulated by the difference of the period numbers between the side grating (N) and the top gratings (M). The levorotatory and dextrorotatory characteristics can be seen in the Fig. 7(b). Beams with larger l can be generated from an OAM beam laser. Larger radius of the microcavity is desired for improving the charge number of the OAM beam laser.

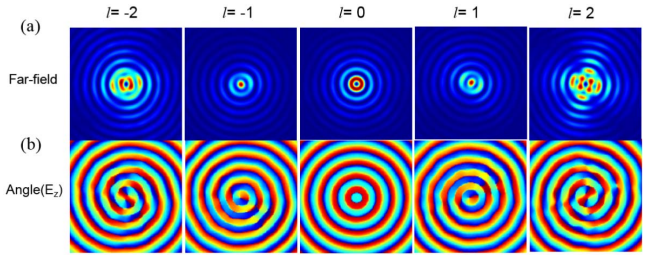

Fig. 7. (a) Simulated far-field intensity and (b) phase pattern in the propagating direction of the near-field of the OAM beam laser. Various orders of −2, −1, 0, 1, and 2 from left to right are displayed.

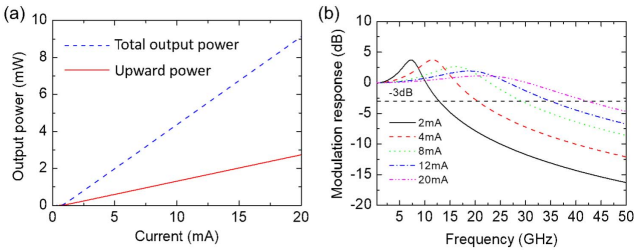

Fig. 8. (a) *L-I* curves at the wavelength of 1310 nm, where both the total output power and the upward part are shown; (b) small signal modulation response of the OAM beam laser at different bias currents.

Noting that, to obtain a travelling-wave wavefront, N-pad metal cannot have a symmetrical boundary with the side grating.

The OAM beam laser can be easily realized at any wavelength by designing the period number of the gratings. The laser can also be realized with transverse magnetic (TM) WGMs with tensile-strained quantum wells, while the emission would be azimuthally polarized.

The characteristics of the OAM beam laser are analyzed by solving the transient multi-mode rate equations[20]. The laser structure with simulation parameters is shown in Fig. 2. The period number of the side and the top gratings is 86 and 85, respectively. All parameters used in the simulation are listed in Table 1.

Table 1. Parameters used in the simulation.

Parameter	Value
Active region thickness (nm)	48
Microcylinder diameter (μm)	12
Current injection width (μm)	1.5
Nonlinear gain saturation factor (10^{-23})	2
Material gain parameter (cm^{-1})	2524
Dominant mode *Q* factor	5100
Transparent carrier density (10^{24} m^{-3})	2
Optical confinement factor	0.1
Group index	3.6
Internal loss of active region (cm^{-1})	20
Surface recombination velocity (10^4 cm/s)	5
Linear recombination coefficient (10^8 s^{-1})	1
Bimolecular recombination coefficient (10^{-10} cm^3/s)	1
Auger recombination coefficient (10^{-29} cm^6/s)	3.5
Spontaneous emission coefficient	0.01
Current injected into the active region (mA)	10
Current injection efficiency	0.8

Here, the dominant mode (*Q* factor is about 5100 in Fig. 5) and other adjacent WGMs are considered in the simulation. In order to make the simulation reliable, actually measured gain parameters are used.

The upward emission takes a ratio of about 30% of the total emitted power. The calculated *L-I* curves are presented in Fig. 8(a), where the upward emitted power has a slope efficiency of 0.142 mW/mA. The threshold current is about 0.766 mA. Therein the linear recombination, spontaneous emission, Auger recombination, surface recombination, and current leakage have contributions of 0.093, 0.2265, 0.1897, 0.1543, and 0.1025 mA, respectively.

The small signal modulation response of the laser under different driving currents is simulated with the results shown in Fig. 8(b). As can be seen, the 3 dB bandwidth of the laser can reach about 20 and 29 GHz at the current injection of 4 and 8 mA, respectively.

4. Summary

In summary, we have theoretically and numerically demonstrated a new design of directly modulated single-mode OAM beam laser. The top gratings including the real part and the imaginary part modulation scatter the WGMs unidirectionally circulating only in clockwise or counterclockwise direction. Meanwhile, the side grating can select a radially polarized standing mode as the lasing mode with little scattering loss. Then an asymmetrical N-pad metal on the top of the microcavity is used for current injection. With the cooperation of the gratings, the OAM beam laser can work with single-mode stably and emit radially polarized emissions vertically. The OAM beam laser can be realized at any wavelength bands and firstly realized with high-speed direct modulation in order to satisfy the applications in optical communications.

Acknowledgement

This work was supported by the National Key Research and Development Program of China (No. 2016YFB0402304).

References

1. L. Allen, M. W. Beijersbergen, R. J. C. Spreeuw, and J. P. Woerdman, "Orbital angular momentum of light and the transformation of Laguerre-Gaussian laser modes," Phys. Rev. A **45**, 8185 (1992).
2. J. Wang, J. Y. Yang, I. M. Fazal, N. Ahmed, Y. Yan, H. Huang, Y. Ren, Y. Yue, S. Dolinar, M. Tur, and A. E. Willner, "Terabit free-space data transmission employing orbital angular momentum multiplexing," Nat. Photon. **6**, 488 (2012).
3. G. M. Terriza, J. P. Torres, and L. Torner, "Twisted photons," Nat. Phys. **3**, 305 (2007).
4. A. Mair, A. Vaziri, G. Weihs, and A. Zeilinger, "Entanglement of the orbital angular momentum states of photons," Nature **412**, 313 (2001).
5. C. Zhang, F. Pang, H. Liu, L. Chen, J. Yang, J. Wen, and T. Wang, "Highly efficient excitation of LP_{01} mode in ring-core fibers by tapering for optimizing OAM generation," Chin. Opt. Lett. **18**, 020602 (2020).
6. T. Lin, A. Liu, X. Zhang, H. Li, L. Wang, H. Han, Z. Chen, X. Liu, and H. Lü, "Analyzing OAM mode purity in optical fibers with CNN-based deep learning," Chin. Opt. Lett. **17**, 100603 (2019).
7. M. Scaffardi, M. N. Malik, E. Lazzeri, G. Meloni, F. Fresi, L. Poti, N. Andriolli, I. Cerutti, C. Klitis, L. Meriggi, N. Zhang, M. Sorel, and A. Bogoni, "A silicon microring optical 2 × 2 switch exploiting orbital angular momentum for interconnection networks up to 20 Gbaud," J. Lightwave Technol. **35**, 3142 (2017).
8. J. Zhang, C. Z. Sun, B. Xiong, J. Wang, Z. B. Hao, L. Wang, Y. J. Han, H. T. Li, Y. Luo, Y. Xiao, C. Q. Yu, T. Tanemura, Y. Nakano, S. M. Li, X. L. Cai, and S. Y. Yu, "An InP-based vortex beam emitter with monolithically integrated laser," Nat. Commun. **9**, 2652 (2018).
9. R. Li, X. Feng, D. Zhang, K. Cui, F. Liu, and Y. D. Huang, "Radially polarized orbital angular momentum beam emitter based on shallow-ridge silicon microring cavity," IEEE Photon. J. **6**, 2200710 (2014).
10. X. Cai, J. Wang, M. J. Strain, B. Johnson-Morris, J. Zhu, M. Sorel, J. L. O'Brien, M. G. Thompson, and S. Yu, "Integrated compact optical vortex beam emitters," Science **338**, 363 (2012).
11. H. Li, D. B. Phillips, X. Wang, Y. D. Ho, L. Chen, X. Zhou, J. Zhu, S. Yu, and X. Cai, "Orbital angular momentum vertical-cavity surface-emitting lasers," Optica **2**, 547 (2015).
12. P. Miao, Z. Zhang, J. Sun, W. Walasik, S. Longhi, N. M. Litchinitser, and L. Feng, "Orbital angular momentum microlaser," Science **353**, 464 (2016).
13. X. Ma, Q. A. Chen, Q. Y. Lu, and W. H. Guo, "Grating assisted microcylinder surface-emitting laser," J. Lightwave Technol. **34**, 4999 (2016).
14. X. Ma, S. Zheng, Q. Chen, S. Tan, P. Zhang, Q. Lu, J. Wang, and W. Guo, "High-speed directly modulated cylindrical vector beam laser," ACS Photon. **6**, 3261 (2019).
15. L. Feng, Y.-L. Xu, W. S. Fegadolli, M.-H. Lu, J. E. B. Oliveira, V. R. Almeida, Y.-F. Chen, and A. Scherer, "Experimental demonstration of a unidirectional reflectionless parity-time metamaterial at optical frequencies," Nat. Material. **12**, 108 (2013).
16. Y.-D. Yang and Y.-Z. Huang, "Symmetry analysis and numerical simulation of mode characteristics for equilateral-polygonal optical microresonators," Phys. Rev. A **76**, 023822 (2007).
17. W. B. Zimmerman, *Multiphysics Modeling with Finite Element Method* (University of Sheffield, 2006).
18. A. Taflove and S. C. Hagness, *Computational Electrodynamics: the Finite-Difference Time-Domain Method*, 3rd ed. (Artech House, 2005).
19. W. H. Guo, W. J. Li, and Y. Z. Huang, "Computation of resonant frequencies and quality factors of cavities by FDTD technique and Padé approximation," IEEE Microwave Wireless Compon. Lett. **11**, 223 (2001).
20. L. A. Coldren, S. W. Corzine, and M. L. Mashanovitch, *Diode Lasers and Photonic Integrated Circuits*, 2nd ed. (Wiley, 2012).